



**HAL**  
open science

# Non-Typical Supershear Rupture: Fault Heterogeneity and Segmentation Govern Unilateral Supershear and Cascading Multi-Fault Rupture in the 2021 Mw $M_w$ 7.4 Maduo Earthquake

J. Hayek, M. Marchandon, D. Li, L. Pousse-Beltran, James Hollingsworth, T. Li, A.-a. Gabriel

## ► To cite this version:

J. Hayek, M. Marchandon, D. Li, L. Pousse-Beltran, James Hollingsworth, et al.. Non-Typical Supershear Rupture: Fault Heterogeneity and Segmentation Govern Unilateral Supershear and Cascading Multi-Fault Rupture in the 2021 Mw  $M_w$ 7.4 Maduo Earthquake. *Geophysical Research Letters*, 2024, 51 (20), pp.e2024GL110128. 10.1029/2024GL110128 . hal-04798413

**HAL Id: hal-04798413**

**<https://hal.science/hal-04798413v1>**

Submitted on 22 Nov 2024

**HAL** is a multi-disciplinary open access archive for the deposit and dissemination of scientific research documents, whether they are published or not. The documents may come from teaching and research institutions in France or abroad, or from public or private research centers.

L'archive ouverte pluridisciplinaire **HAL**, est destinée au dépôt et à la diffusion de documents scientifiques de niveau recherche, publiés ou non, émanant des établissements d'enseignement et de recherche français ou étrangers, des laboratoires publics ou privés.



Distributed under a Creative Commons Attribution 4.0 International License

# Geophysical Research Letters<sup>®</sup>

## RESEARCH LETTER

10.1029/2024GL110128

### Key Points:

- We present new high-resolution optical correlation displacement analysis, joint geodetic slip, and multi-segment 3D dynamic rupture models
- A preferred model has multi-peak moment rate release, unilateral double-onset supershear rupture, and dynamic triggering of two faults
- Complex fault geometry, prestress heterogeneity, and fracture energy variability drive supershear transition and off-fault damage pattern

### Supporting Information:

Supporting Information may be found in the online version of this article.

### Correspondence to:

A.-A. Gabriel,  
algabriel@ucsd.edu

### Citation:

Hayek, J. N., Marchandon, M., Li, D., Pousse-Beltran, L., Hollingsworth, J., Li, T., & Gabriel, A.-A. (2024). Non-typical supershear rupture: Fault heterogeneity and segmentation govern unilateral supershear and cascading multi-fault rupture in the 2021  $M_w$  7.4 Maduo earthquake. *Geophysical Research Letters*, 51, e2024GL110128. <https://doi.org/10.1029/2024GL110128>

Received 9 MAY 2024  
Accepted 28 AUG 2024

© 2024. The Author(s).

This is an open access article under the terms of the [Creative Commons Attribution License](#), which permits use, distribution and reproduction in any medium, provided the original work is properly cited.

## Non-Typical Supershear Rupture: Fault Heterogeneity and Segmentation Govern Unilateral Supershear and Cascading Multi-Fault Rupture in the 2021 $M_w$ 7.4 Maduo Earthquake

J. N. Hayek<sup>1</sup> , M. Marchandon<sup>1</sup> , D. Li<sup>1,2</sup> , L. Pousse-Beltran<sup>3</sup> , J. Hollingsworth<sup>3</sup> , T. Li<sup>4,5</sup> , and A.-A. Gabriel<sup>1,6</sup> 

<sup>1</sup>Ludwig-Maximilians-Universität München, Munich, Germany, <sup>2</sup>GNS Science, Lower Hutt, New Zealand, <sup>3</sup>Université Grenoble Alpes, Université Savoie Mont Blanc, CNRS, IRD, University Gustave Eiffel, ISTerre, Grenoble, France, <sup>4</sup>State Key Laboratory of Earthquake Dynamics, Institute of Geology, China Earthquake Administration, Beijing, China, <sup>5</sup>Xinjiang Pamir Intracontinental Subduction National Observation and Research Station, Beijing, China, <sup>6</sup>Scripps Institution of Oceanography, UC San Diego, La Jolla, CA, USA

**Abstract** Previous geodetic and teleseismic observations of the 2021  $M_w$  7.4 Maduo earthquake imply surprising but difficult-to-constrain complexity, including rupture across multiple fault segments and supershear rupture. Here, we present an integrated analysis of multi-fault 3D dynamic rupture models, high-resolution optical correlation analysis, and joint optical-InSAR slip inversion. Our preferred model, validated by the teleseismic multi-peak moment rate release, includes unilateral eastward double-onset supershear speeds and cascading rupture dynamically triggering two adjacent fault branches. We propose that pronounced along-strike variation in fracture energy, complex fault geometries, and multi-scale variable prestress drives this event's complex rupture dynamics. We illustrate how supershear transition has signatures in modeled and observed off-fault deformation. Our study opens new avenues to combine observations and models to better understand complex earthquake dynamics, including local and potentially repeating supershear episodes across immature faults or under heterogeneous stress and strength conditions, which are potentially not unusual.

**Plain Language Summary** The mechanism of cascading rupture and supershear propagation, when fault moves faster than in situ shear wave speed on multiple fault segments, remains unclear. On 22 May 2021, a magnitude 7.4 strike-slip earthquake occurred in central-east Tibet with episodic supershear suggested by geodetic and seismological inversions. Here, we build a physics-based 3D fully dynamic model, informed by regional tectonics, geomorphology, and high-resolution geodetic data, to better understand the earthquake's behavior and its implications for seismic hazards. The preferred rupture scenario reproduces key features, such as multi-peak moment release, asymmetric supershear fronts, and dynamic triggering of secondary fault branches. Our model suggests that regional stress field, geometric complexity, and the along-strike variation of frictional properties are crucial for earthquake dynamics and coseismic surface damage patterns. Our mechanically viable model offers insights into a comprehensive knowledge of rupture complexity and regional seismic hazard assessment.

## 1. Introduction

On 22 May 2021, the Maduo earthquake, a  $M_w$  7.4 strike-slip event, struck the northeastern Tibetan Plateau (Figure 1a), affecting the local population (UNICEF China, 2021) and infrastructure (e.g., M. Zhu et al., 2023). The earthquake ruptured the eastern segment of the Kunlun Mountain Pass–Jiangcuo Fault (KMPJF), a NW-trending left-lateral strike-slip branch fault south of the East Kunlun fault bounding the Bayan Har Block (Guo et al., 2021). The 2021 Maduo event is the largest earthquake in China since the 2008  $M_w$  7.9 Wenchuan earthquake (Figure 1a) and resulted in complex surface rupture (Pan et al., 2022; Z. Yuan et al., 2022).

The major strike-slip faults surrounding the Bayan Har block all hosted large earthquakes with magnitudes >6.5 in China since 1997 (L. Huang et al., 2021; P. Zhang et al., 2003; Y. Zhu et al., 2021). In contrast, no major earthquake occurred on the KMPJF, which does not have a clear geomorphological expression and was only partly mapped before the Maduo earthquake (Z. Yuan et al., 2022).

Previous studies focused on analyzing the static, kinematic, and dynamic source properties of the Maduo earthquake using geodetic, teleseismic, and field data (Gao et al., 2021; L. He et al., 2021; Guo et al., 2021; Jin & Fialko, 2021;

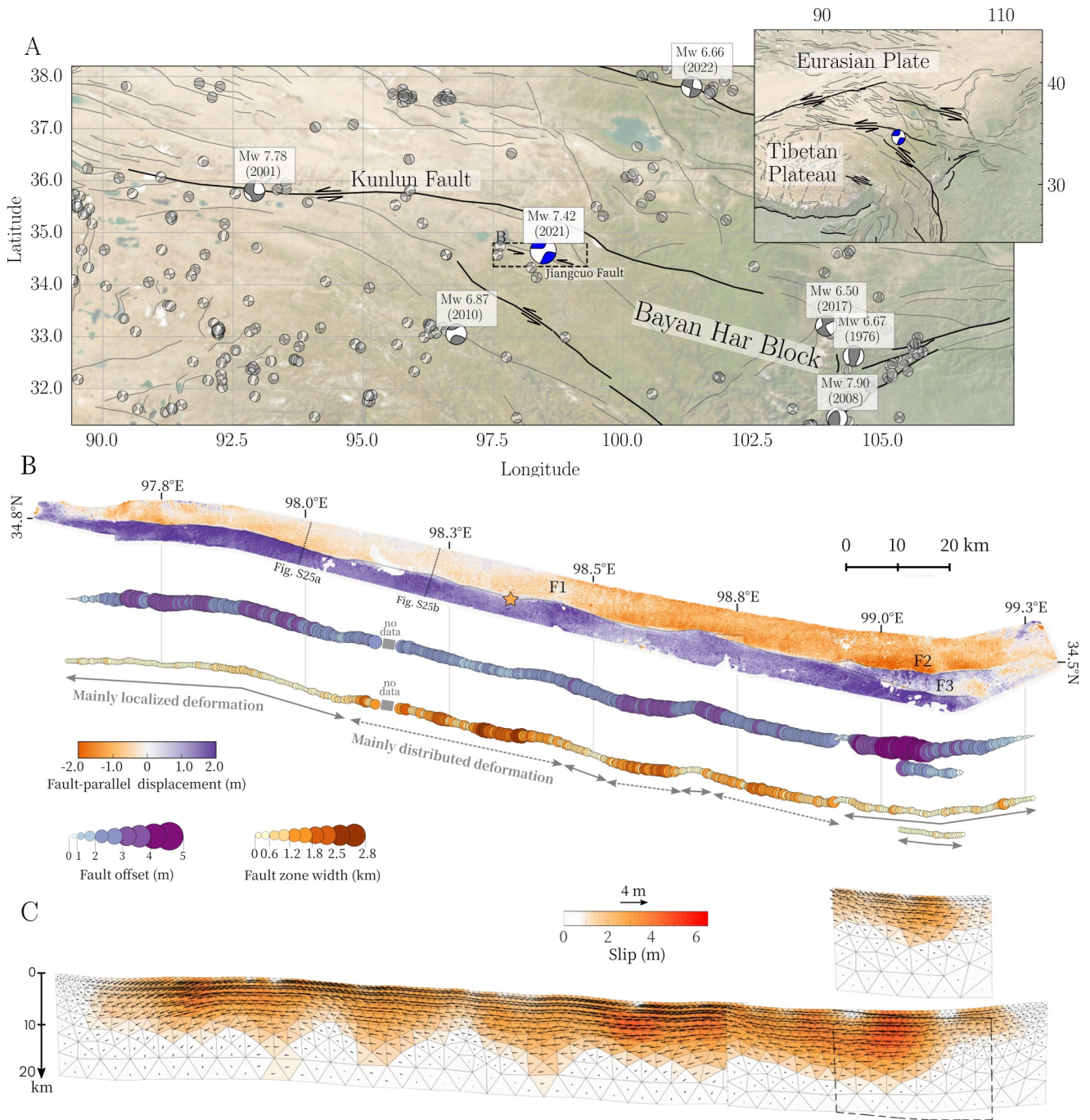


**Figure 1.** (a) Tectonic setting of the study area showing the regional active faults of the Tibet Plateau (black lines, (Styron et al., 2010)) and the moment tensor mechanisms of past earthquakes (gray beachballs, extracted from the global Central Moment Tensor database (Dziewonski et al., 1981; Ekström et al., 2012)).  $M_w \geq 6.5$  focal mechanisms are labeled and highlighted using larger beachball diagrams. Superimposed is the 2021  $M_w 7.4$  Maduo earthquake USGS moment tensor mechanism (blue). The top-right inset shows a zoom-out view of the study area. (b) Top: Surface fault-parallel displacement field of the  $M_w 7.4$  Maduo event inferred from the correlation of SPOT-6 optical satellite imagery (Supporting Information S1). The gray lines indicate the surface fault traces extracted from the fault-parallel displacement field and the dotted black lines locate the profiles shown in Figure S5 in Supporting Information S1. Middle and bottom: Fault offsets and fault zone width along the fault strike measured from the fault-parallel surface displacement field. (c) Slip amplitude and rake for the Maduo earthquake estimated from a joint inversion of InSAR and optical data. The assumed fault geometry comprises one main fault and two branching segments in the east, consistent with the dynamic rupture simulation.

Pan et al., 2022; Ren et al., 2021; G. Wei et al., 2023; Yue et al., 2022; J. Yuan & Li, 2023; Yuan & Li, 2023). Most joint inversions, combining geodetic and teleseismic observation, agree on the earthquake propagating across multiple fault segments with varying rupture speeds (e.g., K. He et al., 2021; Jin & Fialko, 2021; S. Wang et al., 2022;

Yue et al., 2022). The rupture speed inferred for the eastward-propagating front falls in the range of 3–5 km/s (Q. Li et al., 2022; Yue et al., 2022; X. Zhang et al., 2022) whereas the westward propagation is inferred as 2.5–2.8 km/s (Chen et al., 2022; S. Wei et al., 2022). However, the mechanical relationship between potential supershear rupture episodes and regional tectonics remains highly debated, partially due to the non-uniqueness of the results from various data-driven and physics-based models (Chen et al., 2022; Fang et al., 2022; S. Wei et al., 2022; Yue et al., 2022; X. Zhang et al., 2022).

Geometrically complex fault systems, such as the KMPJF, may be expected to host smaller and slower earthquakes compared to more mature faults (Cappa et al., 2014; Y. Huang et al., 2014; Manighetti et al., 2015; Perrin et al., 2016; Schwartz & Coppersmith, 1984), rendering the magnitude and inferred kinematic complexity of the Maduo earthquake surprising. However, several sizable strike-slip earthquakes have occurred across geometrically complex faults including the 1992 Landers, the 2016 Kaikoura, the 2019 Ridgecrest, and the 2023 Kahramanmaraş earthquakes (Gabriel et al., 2023; Hauksson et al., 1993; Hamling et al., 2017; Ross et al., 2019). The complexity of the KMPF is evident in the coseismic surface damage distribution, as constrained by geodetic observations (C. Li, Li, Hollingsworth, et al., 2023; C. Li, Li, Shan, & Zhang, 2023) and field measurements (Z. Yuan et al., 2022). The details of the surface rupture expression may correlate with subsurface rupture dynamics, multi-fault interaction, fault orientation with respect to the regional stress field and near-fault plasticity (Jara et al., 2021; Liu-Zeng et al., 2024; Rodriguez Padilla & Oskin, 2023; Taufiqurrahman et al., 2023; Wen et al., 2024; Wollherr et al., 2019).

Together with a new analysis of high-resolution optical SPOT-6/7 data, the 2021 Maduo earthquake provides a unique opportunity to understand the underlying physics of multi-segment bilateral rupture across a complex fault system and related observables. We demonstrate that combining high-resolution optical and InSAR data analysis with 3D multi-fault dynamic rupture simulations can constrain dynamically viable pre- and co-seismic fault system mechanics and help reduce the non-uniqueness in earthquake source observations.

Our study combines 3D dynamic rupture simulations with joint optical and InSAR geodetic source inversion and surface damage measurements. The simulations incorporate optically derived multi-segment non-planar fault geometry, data-constrained heterogeneous initial stress, off-fault Drucker-Prager plasticity, strong velocity-weakening rate-and-state friction, topography, and 3D subsurface velocity structure. Our preferred model reproduces the observed characteristics of the Maduo earthquake, such as multi-peak moment rate release, heterogeneous fault slip distribution, and multi-fault rupture. We compare the modeled co-seismic distribution of off-fault deformation with fault damage from surface geodetic measurements and identify geodetic off-fault signatures of supershear rupture onset. We illustrate the importance of key model ingredients by contrasting them with less optimal rupture scenarios. We propose that along-strike variations in fracture energy and fault geometry and 3D variable multi-scale prestress govern the complex multi-segment rupture dynamics and favor unilateral double-onset supershear propagation.

## 2. Methods

### 2.1. Geodetic Analysis

We perform joint InSAR (Sentinel-1 imagery) and optical geodetic analysis of the Maduo earthquake. We measure the horizontal surface displacement field from the correlation of high-resolution SPOT-6/7 satellite imagery (Figures 1b and Supporting Information S1). This allows us to map the surface rupture traces and analyze the pattern of near-fault deformation. We infer a main segment (F1 in Figure 1b) connected to a shorter segment (F2) via a restraining step-over and a third smaller segment (F3), branching south-eastward from the main segment. We measure the amount and variability of surface fault slip and fault zone width from stacked perpendicular profiles of the SPOT-6/7 surface displacement field, regularly spaced along the fault strike (Supporting Information S1). Assuming a homogeneous elastic half-space, we combine Sentinel-2 optical data at a resolution of 40 m with InSAR data to infer the static slip distribution at depth from a constrained least-square inversion (Figures S1–S4 in Supporting Information S1). Here, all faults are assumed 83°N dipping for simplicity (Figure S2 in Supporting Information S1). Note that this constant-dip-angle assumption does not impact significantly the inferred slip distribution (Figures S6 and S7 in Supporting Information S1).

## 2.2. 3D Dynamic Rupture Simulations

We simulate 3D dynamic rupture across multiple fault segments and the associated seismic wave propagation using the open-source software *SeisSol* (Heinecke et al., 2014; Käser & Dumbser, 2006; Pelties et al., 2014; Uphoff et al., 2017, Supporting Information S1). Dynamic rupture models require initial conditions, including fault geometry, prestress, frictional fault strength, and subsurface elastic and plastic material properties (Gabriel et al., 2023; Harris et al., 2018; Ramos et al., 2022).

We construct the fault geometry by extruding the geodetically inferred surface fault traces at depth, assuming variable dip angles constrained from a systematic geodetic sensitivity analysis (Text S2 and Figure S6 in Supporting Information S1) and relocated aftershock distributions (W. Wang et al., 2021). In our preferred dynamic rupture model, we assume a northward-dipping angle of  $83^\circ$  for the main fault segment, and  $85^\circ$  south for the segments F2 and F3. Segment F2 is shallowly connected to the main segment, while F3 is disconnected. Our constructed fault geometries for segments F1 and F3 agree with most previous studies. The assumed sub-vertical south-dipping dip-angle of segment F2 is consistent with aftershock distributions (Fan et al., 2022; K. He et al., 2021; Jin et al., 2023; W. Wang et al., 2021; S. Wei et al., 2022) but inconsistent with estimates based on geodetic data (Chen et al., 2022; Jin & Fialko, 2021; G. Wei et al., 2023; Zhao et al., 2021, and Text S2, Figure S6 in Supporting Information S1). However, an alternative dynamic rupture scenario in which all segments are  $83^\circ$  N dipping fails to rupture segments F2 and F3 (Figure S18 in Supporting Information S1).

Our assumed prestress is depth-dependent and multi-scale; we combine a laterally uniform ambient tectonic loading resembling the regional stress state with geodetically constrained small-scale on-fault stress heterogeneities and depth-dependent normal stress. The resulting combined on-fault and off-fault initial shear and normal stress distribution are heterogeneous on the scale of the non-planar fault geometry.

We set a uniform non-Andersonian homogeneous background stress orientation (Figures S8A–S8C and S9 in Supporting Information S1) guided by regional moment tensor inversion (B. Xu & Zhang, 2023). This prestress resembles sinistral strike-slip faulting with the maximum compressive stress direction  $S_{Hmax} = N78^\circ E$  and the stress shape ratio  $\nu = 0.5$ . We assume depth-dependent effective normal stresses following a hydrostatic gradient characterized by a pore fluid-pressure ratio of  $\gamma = \rho_{water}/\rho_{rock} = 0.37$  (Figure S10A in Supporting Information S1). While all fault segments vertically extend to 20 km depth, we mimic the brittle-ductile transition at  $\sim 10$  km by smoothly reducing deviatoric stresses to zero (Figure S10B in Supporting Information S1, Ulrich et al., 2019).

In addition to the regional ambient prestress, which is modulated by the non-planar fault geometry (e.g., Biemiller et al., 2022), we add small-scale prestress variability inferred from our geodetic slip model (Text S3 in Supporting Information S1; Jia et al., 2023; Tinti et al., 2021). The geodetically inferred prestress variability enhances the shear stresses in optimally oriented portions of the fault by a maximum of  $\sim 3$  MPa within the seismogenic zone (Figure S9A in Supporting Information S1). It also reduces the shear stress at strong geometrical bends by  $\sim 1$  MPa, while generally increasing the normal stresses up to 2.9 MPa on F3 (Figure S9B in Supporting Information S1). On-fault pre-stress heterogeneities modulate but do not drive rupture dynamics or the final slip distribution as illustrated in an alternative dynamic rupture scenario without prestress heterogeneities (Figures S12 and S13 in Supporting Information S1).

A fast velocity-weakening rate-and-state friction law governs the strength of all faults (Dunham et al., 2011a; Gabriel et al., 2012). All friction parameters are listed in Table S1 in Supporting Information S1. We include a 1 km shallow velocity-strengthening layer (Figure S8E in Supporting Information S1). This is a simplifying assumption, as the observed early afterslip occurs within the top 2–3 km of the upper crust and varies along-strike (Fang et al., 2022; Jin et al., 2023). However, a dynamic rupture model with a 3 km deep velocity-strengthening layer fails to activate F3 (Text S6 and Figure S14 in Supporting Information S1).

The seismic  $S$  parameter (Aki & Richards, 2002; Andrews, 1976; Dunham, 2007) characterizes the relative fault strength governing dynamic rupture propagation and arrest by balancing fracture energy and strain energy release (Cocco et al., 2023). It is defined as the ratio between the peak and residual strengths,  $\tau_p$  and  $\tau_r$  relative to the background level of initial loading  $\tau_0$ , so that  $S = (\tau_p - \tau_0)/(\tau_0 - \tau_r)$ . In our framework, complex initial stress and fault geometries modulate the closeness to failure before the onset of rupture and the relative fault strength.

We allow for the characteristic slip distance  $D_{RS}$  to vary along-strike as a proxy for heterogeneous fracture energy, enabling us to vary it independently of the  $S$  parameter. Fracture energy fundamentally affects dynamic rupture nucleation, propagation and arrest, and is potentially inferrable from seismological observations (Abercrombie, 2021).

We account for regional 3D velocity structure (Xin et al., 2018), with a resolution of  $0.5^\circ$  laterally and 5 km resolution with depth (Figure S8D in Supporting Information S1). We include off-fault plasticity described by non-associative Drucker-Prager visco-plastic rheology (Andrews, 2005; Wollherr et al., 2018). We use a bulk friction coefficient of 0.5 and a bulk plastic cohesion  $C_{off}$  proportional to the 3D variable shear modulus  $\mu$  as  $C_{off} = 2 \times 10^{-4} \mu$  (Table S1 in Supporting Information S1) throughout the entire domain (Roten et al., 2014; Taufiqurrahman et al., 2023). The volumetric bulk initial stresses governing off-fault plasticity are the same as the depth-dependent, laterally uniform ambient tectonic prestress.

### 3. Results

#### 3.1. Heterogeneous Near-Surface Deformation and Homogeneous Fault Slip at Depth From Joint Geodetic Analysis

The 6 m resolution SPOT 6/7 fault-parallel displacement field shown in Figure 1b reveals a highly heterogeneous deformation pattern along the rupture trace. Deformation ranges from very localized ( $<0.6$  km), that is, sharp discontinuities in the surface displacement field in the vicinity of the fault, to broader shear zones ( $>1.8$  km), that is, more gradual displacement changes across a wider fault zone (Figure S5 in Supporting Information S1). This is reflected in strong variations of our measured fault zone width along strike (Figure 1b).

Westward of the epicenter, surface deformation can be divided into two distinct regions: (a) A 30 km long segment where deformation is broadly distributed, characterized by an average fault zone width of 1,538 m; (b) a 40 km segment at the western end of the rupture, where deformation is highly localized, and the mean fault zone width is 425 m. Eastward of the epicenter, surface deformation is more heterogeneous. We identify three areas of localized deformation with a mean fault zone width of 747, 587, and 568 m, from west to east, respectively. These are separated by two areas of distributed deformation with a mean fault zone width of 1,660 and 1,213 m, respectively.

We infer considerable surface fault offsets (Figure 1b) of 2.44 m on average. The fault offsets tend to be larger where deformation is localized. However, there are exceptions, for example, near latitude  $98.65^\circ\text{E}$ . We identify three distinct regions of high surface slip located at the western and eastern ends of the rupture surface expression, respectively, and near longitude  $98.65^\circ\text{E}$ .

Our joint InSAR Sentinel-1 and optical Sentinel-2 geodetic slip model is shown in Figure 1c and features overall smooth, shallow ( $<10$  km depth) and high-amplitude fault slip, in agreement with previous geodetic and teleseismic slip models (e.g., Jin & Fialko, 2021; Q. Li et al., 2022). We resolve three areas of large slip reaching 6 m and a significant dip-slip component at the western end of fault segment F1. Slip across segment F3 is, on average, lower and shallower than for the two main fault segments, F1 and F2.

We use our joint geodetic analysis to inform and verify a suite of dynamic rupture simulations. Subsequently, we discuss signatures of rupture complexity in the on- and off-fault geodetic data.

#### 3.2. Multi-Fault 3D Dynamic Rupture Scenarios

To find a preferred rupture scenario, we explore an ensemble of more than 100 dynamic rupture scenarios varying fault fracture energy, off-fault material strength, prestress, and fault segmentation. We initiate all rupture scenarios at the USGS hypocenter (Supporting Information S1). Our preferred model features cascading dynamic rupture across multiple segments and double-onset, unilateral supershear along the eastern faults (Figure 2). It matches key observed characteristics of the event, including the multi-peak moment rate release and the overall on-fault slip distribution (Figures 2a and 2b).

Figure 2a compares the dynamic rupture moment rate release with teleseismic inferences by the USGS and Chen et al. (2022). Our preferred model has a total seismic moment of  $0.98 \times 10^{20}$  N m, equivalent to an on-fault moment magnitude of  $M_w 7.26$ . Our modeled on-fault moment rate release resembles the two major peaks of the USGS source time function at 13 and 20 s, within the expected uncertainties. Overall, the teleseismic

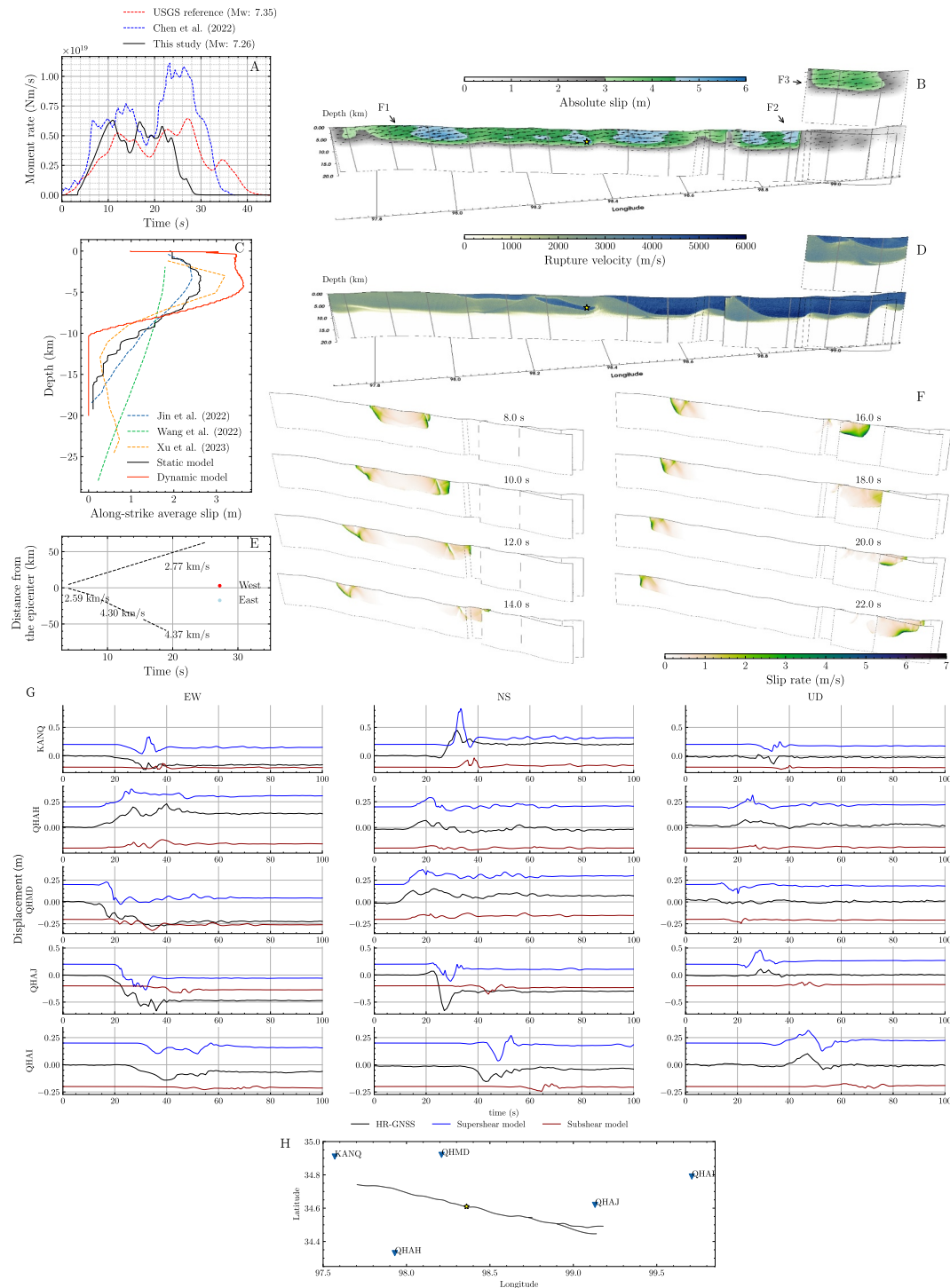


**Figure 2.** (a) Modeled moment rate function of the preferred dynamic rupture scenario for the 2021  $M_w$  7.4 Maduo earthquake (black). The finite fault moment rate functions from USGS (2021) and Chen et al. (2022) are shown as red and blue dashed lines, respectively. (b) Modeled fault slip amplitude on the fault segments (F1, F2, and F3) in a three-dimensional perspective view. Fault slip along segment F3, which is located close to F2, is shown in the top inset. The vertical axis indicates the depth below the Plateau surface from 0 to 20 km. Black vectors indicate the slip direction of the rupture front (rake). Contour lines every 10 km from the epicenter are indicated as gray solid lines on the fault. (c) Comparison of the distribution of average slip with depth for our dynamic and static models as well as other published slip models. (d) Distribution of the rupture velocity on the fault. (e) Rupture velocities of westward and eastward propagating fronts with distance from the epicenter, along a transect at 3.5 km depth. The rupture velocities estimated along different fault portions are indicated as dashed lines. (f) Snapshots of fault slip rate shown every 2 seconds between  $t = 8.0$  s to  $t = 22.0$  s of simulation time. (g) Comparison of observed displacement components from high-rate GNSS receivers near the fault (Ding et al., 2022) with synthetic data for two dynamic rupture scenarios: unilateral supershear and bilateral subshear propagation (see Text S10 in Supporting Information S1 for an extended comparison using additional GNSS stations). (h) Map view showing the locations of the GNSS receivers and the surface rupture traces.

inferences have a slightly longer duration, which may be attributed to differences between our on-fault model results and teleseismic inferences, assumed fault geometries and velocity structure, source time functions, and resolution differences.

Our dynamic model results in an average slip  $\sim 1.5$  m larger than the static model (Figures 1c, 2b, and 2c). We observe three sub-regions of high slip accumulation (Figures 1c and 2b), two on the main branch with a maximum slip of 5.2 and 4.8 m, 37 km west and 11 km east of the hypocenter respectively, while the third high slip patch is located on F2 with a max slip of 4.8 m, 40 km east of the hypocenter.

Figures 2d–2e show rupture velocity on the fault and at 3.5 km depth. Spontaneous rupture propagates bilaterally to the northwest and southeast (Figure 2f and Movie S1). While there is limited along-strike variability in seismic wave speeds given by the velocity model, rupture speed varies significantly. The westward rupture front travels at an average speed of  $2.77 \text{ km s}^{-1}$  for 24 s before arresting the edge of the main fault F1 (Figures 2d–2f and Movie S1). We observe early, transient supershear to the west, which is not self-sustained but leads to higher shallower rupture velocities from 12 to 30 km west to the hypocenter at shallow depths ( $<1.9$  km, Figure 2d). The eastward propagating rupture front transitions to supershear speeds twice along the main fault and after “jumping” to fault segment F2 (Figure 2d). At rupture onset, the eastward rupture speed is slightly slower than the westward one with  $2.59 \text{ km s}^{-1}$ , being delayed due to a non-optimally oriented fault bend at the Eastern segment (Figure S8 in Supporting Information S1). After  $\sim 10$  s, the rupture accelerates to  $4.30 \text{ km s}^{-1}$  which is close to the local P-wave speed ( $4.48 \text{ km s}^{-1}$ , Figure 2e). The first transition from subshear to sustained supershear rupture occurs when the rupture front breaks through the free surface 8 km east of the hypocenter (Figures 2d–2f). The surface rupture initiates a supershear transition by P-wave diffraction at the free surface (e.g., Hu et al., 2021; Kaneko & Lapusta, 2010; Tang et al., 2021; J. Xu et al., 2015). The supershear rupture front then dynamically triggers coseismic slip on F2 and F3 at about 14 and 18.5 s, respectively (Figure 2f). The second eastward supershear transition occurs soon after the onset of rupture on F2 at about 45 km along strike from the epicenter (Figure 2d). Eastward rupture then arrests when reaching the eastern end of the third branch at 28 s (Figure 2f). It remains difficult to determine whether supershear rupture during the Maduo earthquake was initiated due to free surface effects or other mechanisms, such as Burridge-Andrews supershear daughter crack nucleation (Andrews, 1985; Burridge, 1973) or rupture jumping (Hu et al., 2016). An alternative dynamic rupture model, which dampens the free surface effect by using a 3 km deep velocity strengthening layer (Text S6 and Figure S14 in Supporting Information S1), preserves supershear rupture across the east part of the fault system, but the rupture does not propagate to F3.

We find that a decrease in characteristic slip distance  $D_{RS}$  for 20 km along-strike the eastern main fault away from the hypocenter (Figure S8F in Supporting Information S1) is required to facilitate dynamic triggering of the southernmost fault branches F2 and F3. In our preferred model, the relatively high prestress around the nucleation area promotes initial supershear fronts in both directions, while only the propagating front along the eastern fault sustains. There, locally lower  $D_{RS}$  decreases fracture energy (Cocco et al., 2023), favors supershear rupture speeds, and increases dynamically accumulating fault slip. In Figures S24 and S26 in Supporting Information S1, we show alternative models with homogeneously small and large  $D_{RS}$  leading to either bilateral sub- or bilateral supershear rupture, respectively (Text S9 in Supporting Information S1). Both models fail to rupture all fault segments and cannot reproduce neither the characteristic moment rate release peaks nor their duration. Furthermore, both models generate large off-fault plasticity in the western section of the fault system, which does not compare well to observations (Section 3.3, Figure 3, and Figures S25 and S27 in Supporting Information S1).

We illustrate the significance of incorporating off-fault plasticity to match the geodetically observed distribution of off-fault damage in Figures S29 and S31 in Supporting Information S1 (Text S9 in Supporting Information S1). These alternative scenarios have lower and higher bulk plastic cohesion, respectively, affecting the width of the off-fault plastic strain pattern and the rupture energy budget. We illustrate the importance of fault geometries in two exemplary alternative models with varying segmentation and dipping angles in Figures S16 and S18 in Supporting Information S1. When F1 and F2 are modeled as a continuous segment, the rupture succeeds in dynamically activating F3. However the off-fault plastic strain pattern changes toward the easternmost branches (Text S7 in Supporting Information S1). In contrast, segments F2 and F3 are not rupturing in an alternative model where these segments are not continuous but dip  $83^\circ$  northward (Figure S18 in Supporting Information S1).

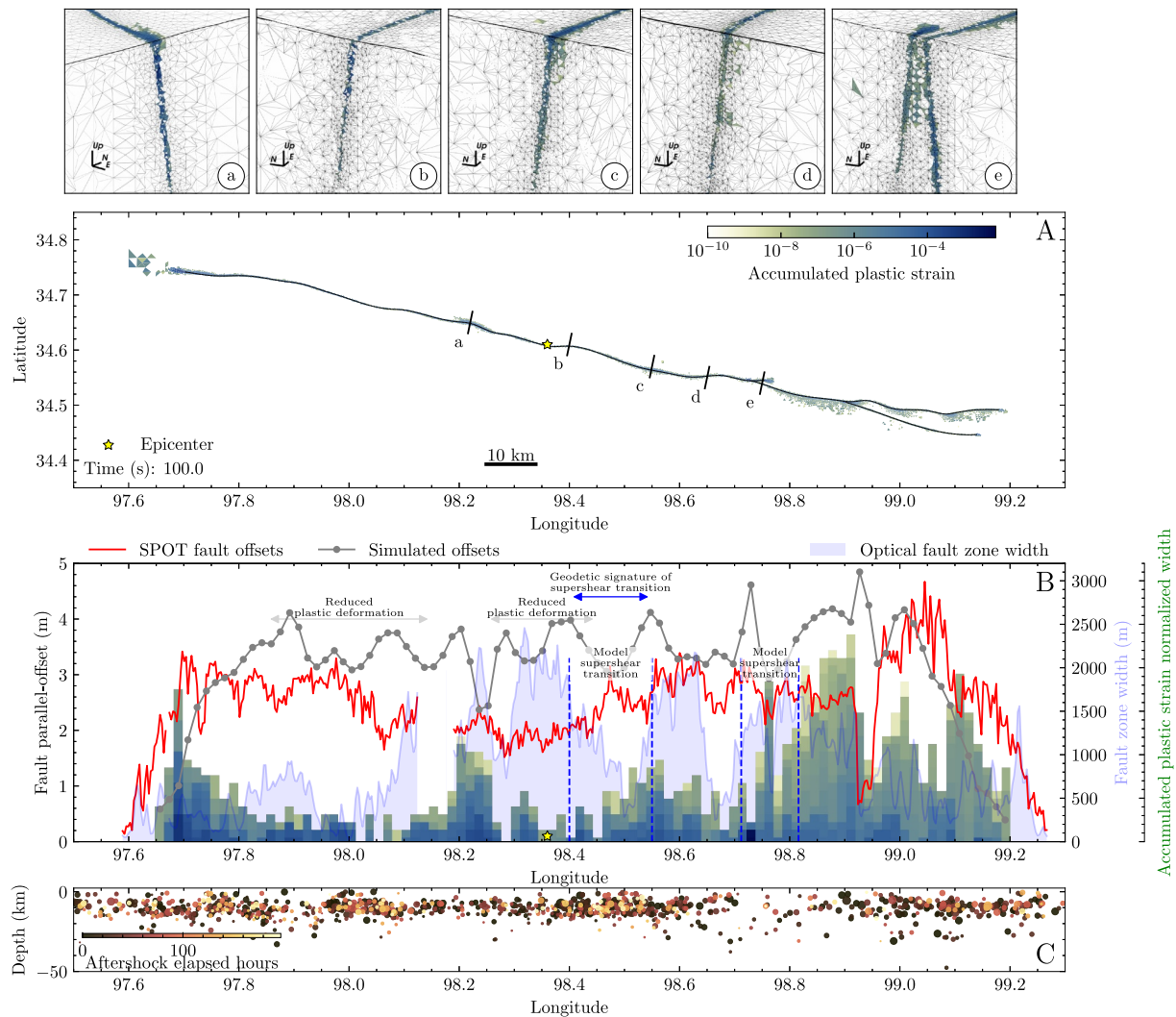


**Figure 3.** (a) Map view of the accumulated plastic strain at the surface at the end of the dynamic rupture simulation. The USGS epicenter is marked with a star. The top-panel insets (a–e) show a three-dimensional perspective view of the plastic strain accumulation at five chosen locations indicated by black lines in panel (a). (b) Comparison of the optically inferred fault-parallel offsets (red) and fault zone width (shaded light blue area) with the simulated fault offsets (gray) and off-fault plasticity (histogram). The histogram depicts the along-strike variation of surface accumulated plastic strain derived from 94 transects along-strike composed of 100 sampling points over a width of 8.88 km. Vertical blue dashed lines mark the two supershear transitions in our preferred model while the horizontal blue line locates the signature of supershear transition in the optical data. (c) Depth versus longitude distribution of aftershocks from the catalog of W. Wang et al. (2021).

The initial conditions of our preferred dynamic rupture model yield highly heterogeneous relative fault strength, as illustrated by the on-fault variability of the  $S$  parameter (Figure S8I in Supporting Information S1). Regions of low  $S < 1.2$  characterize the southeastern faults, facilitating dynamic triggering of the adjacent segments F2 and F3 and favoring local supershear rupture velocities. Several locally stronger fault portions act as barriers, as indicated by higher  $S$  values in the eastern part of the fault system. Figures S20 and S22 in Supporting Information S1 show alternative models with different choices for the ambient stress orientation (Text S8 in Supporting Information S1). A smaller  $S_{Hmax}$  angle ( $S_{Hmax} \approx N68^\circ E$ ) yields larger slip along the F1 and F2 segments (Figure S20 in Supporting Information S1), larger simulated offsets, and larger off-fault deformation at the eastern segments of the fault system (Figure S21 in Supporting Information S1) compared to the preferred model. Larger  $S_{Hmax}$  orientation ( $S_{Hmax} \approx N88^\circ E$ ) results in longer rupture duration and uniformly subshear rupture speeds, reduced on-fault slip, off-fault plastic strain, and simulated offsets, and the inability to dynamically trigger F3 (Figure S22 in Supporting Information S1).

### 3.3. Modeled Off-Fault Deformation

Our dynamically modeled surface deformation matches the GPS observations (M. Wang et al., 2021), although the horizontal components are slightly underestimated (Figures S32A and S32B in Supporting Information S1). We observe the largest misfit in orientation and amplitude at station QHAJ, potentially due to unmodelled local fault zone structures. Our preferred forward simulation also reproduces the surface deformation inferred from both the ascending and descending interferograms, with minor divergence near the fault trace (Figures S32C–S32H in Supporting Information S1).

Figure 2g compares the observed displacement time series from 5 near-fault high-rate GNSS stations (Ding et al., 2022) with our preferred unilateral supershear model and an alternative subshear model (Figure S22 in Supporting Information S1). The arrival time, duration, shape, and amplitude of the displacement time-series are well reproduced by our preferred model. In contrast, the synthetics of the subshear model are systematically lower in amplitude and delayed in timing. This discrepancy is particularly visible for the eastward stations (e.g., QHAJ and QHAI), where the first arrivals in the subshear model are delayed by 15 s compared to the observations, while the preferred supershear model's timing better aligns with the observations with misfits less than 5 s. The better performance of the supershear model is also demonstrated for other medium-distant stations (Figure S33 in Supporting Information S1).

Figure 3a shows a map view and 3D cross-sections of the plastic strain accumulated during the dynamic rupture simulation. The surface distribution of off-fault plastic deformation varies along strike, with a wider distribution observed further away from the epicenter and significant local variations. Analyzing the modeled plastic strain along fault-perpendicular transects (Figure 3b and Text S4 in Supporting Information S1) reveals two zones of reduced deformation width located at 97.85°E–98.15°E and 98.25°E–98.45°E (inset b in Figures 3a and 3b). These zones are separated by local peaks in off-fault plastic deformation corresponding to fault geometrical complexities such as fault kinks and intersections (insets a, c, and e in Figure 3a). In addition, we observe that the plastic strain distribution is strongly asymmetric across the fault. A higher level of plastic strain is observed on the northern part of segment F1, although 3D cross-sections c and d show a subtle southward asymmetry (Figure 3a). In contrast, the modeled off-fault deformation localizes toward the south across segment F2.

## 4. Discussion

### 4.1. Unilateral Supershear and Cascading Dynamic Rupture

The observational evidence for supershear rupture during the Maduo event remains debated. Several studies report asymmetric rupture with supershear velocity to the east from kinematic finite fault inversion and back-projection analysis (Q. Li et al., 2022; Lyu et al., 2022; Yue et al., 2022; X. Zhang et al., 2022). However, bilateral transient supershear episodes have also been inferred using similar methodologies and data sets (Cheng et al., 2023; B. Xu & Zhang, 2023). S. Wei et al. (2022) argue for sustained subshear speed of the entire rupture from back-projection and multiple point source inversion, which is in line with the joint geodetic and teleseismic inversion of Chen et al. (2022). Our geodetically constrained dynamic rupture simulations indicate energetic nucleation and eastward unilateral, cascading supershear rupture speeds with a double transition from sub-to supershear speeds that would complicate observational inferences. The model's average eastward supershear and westward subshear speeds of  $\sim 3.4 \text{ km s}^{-1}$  and  $\sim 2.18 \text{ km s}^{-1}$ , respectively, fall within the range of observational values (2.82–5 and 2–3  $\text{km s}^{-1}$ , respectively, Q. Li et al., 2022; Lyu et al., 2022; Yue et al., 2022; X. Zhang et al., 2022).

Cascading spontaneous rupture dynamically triggering both southeastern fault branches is a key constraint in identifying the dynamic parameters of our preferred simulation. Our models suggest that the dynamic triggering of the eastern branches may not have happened without an eastward supershear rupture front. We demonstrate that along-fault variations in fracture energy can be a key driver of diverse ranges of rupture speeds during the same earthquake. The second onset of eastward supershear rupture is also located at the free surface but aided by dynamic rupture jumping across highly stressed step-over faults of variable dip (Hu et al., 2016; Tang et al., 2021). Wen et al. (2024) analyzed dynamic rupture models with realistic fault geometry and variable regional stresses to demonstrate the impact of compressive stress orientation on fault slip, dynamic triggering, and supershear propagation. Our simulations additionally integrate regional geodetic constraints (C. Li, Li, Hollingsworth, et al., 2023;

C. Li, Li, Shan, & Zhang, 2023) and explore the importance of frictional variability, small-scale heterogeneity in local fault stress and complex off-fault rheology on coseismic rupture dynamics.

#### 4.2. Geodetic Off-Fault Signatures of Rupture Complexity

Quantifying the degree of localization of the near-fault deformation from fault zone width (FZW) measurements can help unravel the mechanical behavior of the shallow crust. However, interpretation of such data is difficult due to several mechanisms superimposing and producing similar off-fault deformation patterns (Nevitt et al., 2020). For example, a wide optically inferred fault zone width can be interpreted either as the elastic bulk response of a localized decrease of slip in the shallow part of the fault (i.e., the shallow slip deficit, Fialko et al., 2005) or as distributed inelastic deformation (Antoine et al., 2021; Fialko et al., 2005; Milliner et al., 2015; Scott et al., 2018). While both mechanisms may occur simultaneously within the crust (Antoine et al., 2021; Fialko et al., 2005; Kaneko & Fialko, 2011; S. Ma, 2008; H. Ma et al., 2022; Nevitt et al., 2020; Roten et al., 2017; Simons et al., 2002), their respective contributions to the observed surface deformation remain difficult to untangle. In addition, a wide fault zone width may also result from the shallow soil response to coseismic rupture.

Here, we compare our geodetic observations of distributed deformation through the estimated FZW with the plastic strain distribution of our preferred dynamic rupture model. In this model, off-fault plastic deformation is generally more widespread in the eastern sections of the fault system due to the higher dynamic stresses induced by the supershear rupture front (Dunham et al., 2011a; Jara et al., 2021). In addition, the plastic strain is mainly located on the compressive side of the fault due to the shallow angle of the maximum compressive stress to the fault ( $\sim 20^\circ$ ) (Templeton & Rice, 2008); and is modulated by the geometric fault strike variations (Dunham et al., 2011b; Wollherr et al., 2019). The simulated distribution of plastic strain remains similar for different plasticity parameterizations (Supporting Information S1), while the amplitude of off-fault plastic strain changes (Figures S29 and S31 in Supporting Information S1).

Our comparison suggests that the optically inferred distributed deformation can be at least partially attributed to off-fault plastic deformation. The measured optical FZW and the modeled plastic deformation width show strikingly similar along-strike variability at several locations (Figure 3): (a) a narrow peak of enlarged fault zone width between  $98.20^\circ$  and  $98.25^\circ$ ; (b) a 10 km long zone of large optical FZW centered on longitude  $98.60^\circ$  coinciding with a peak in the plastic deformation width; and (c) three peaks in the amount of modeled off-fault plasticity on segment F2 correlating with three (less pronounced) peaks in the optical data.

The optical FZW and modeled plastic deformation width also show various disagreements. Near the epicenter, between  $98.3^\circ$  and  $98.45^\circ$ , the optical fault zone width is large, 1800 m on average, whereas our preferred model does not show widespread off-fault plastic deformation. At this particular location, the large optical FZW may partly be attributed to the local geomorphology, which is characterized by Quaternary sand-dunes and swampy terrain where deformation cannot easily localize (Z. Yuan et al., 2022). Moreover, this part of the fault experienced the largest shallow afterslip (Fang et al., 2022), suggesting that the large FZW inferred from our observations may be due to a deficit of shallow slip.

We interpret an observed drastic local reduction of optically inferred fault zone width as a possible geodetic signature of the first supershear transitions of the eastward propagating front. Simpler 2D numerical models have shown that the location of supershear transition can be associated with a sharp local reduction of the damage zone width (Jara et al., 2021; Templeton & Rice, 2008) due to the spatial contraction of the stress field around the rupture tip. In nature, this effect has been observed using high-resolution optical data, albeit once only, for the  $2001M_7.8$  Kunlun earthquake (Jara et al., 2021). The drastic and localized reduction of the optically inferred fault zone width at  $98.5^\circ$  (Figures 1 and 3b) occurs at a straight portion of the fault and does not appear to correlate with variations in the sub-surface material, but does correlate with the first onset of eastward supershear rupture propagation in our preferred dynamic rupture model. The reduction of the modeled off-fault plastic strain width is more gradual in our 3D model than in previous studies, which is likely due to the more gradual onset of supershear rupture at different fault depths (Figure 2d), as well as mixed mode-II-III rupture (Figures 1c and 2b), depth-dependent initial stress (Figures S8A–S8C in Supporting Information S1), heterogeneous fault friction and non-planar, segmented fault geometry (Figures 1c and 2b).

Our results imply that a high level of fault maturity, as well as homogeneous stress-strength conditions and geometric simplicity, may not necessarily be required preconditions for supershear rupture. Local and potentially

repeating supershear episodes across immature faults or under heterogeneous stress and strength conditions have been inferred for the 2023 Turkey earthquake doublet (Abdelmeguid et al., 2023; Delouis et al., 2023; Jia et al., 2023) and may be more common than previously thought.

A remarkable, well-resolved gap in aftershock seismicity (W. Wang et al., 2021) between  $98.65^{\circ}$ – $98.9^{\circ}$  (Figure 3c), which has been proposed to indicate locally high stress release (S. Wei et al., 2022), may provide additional evidence for eastward supershear propagation. Postseismic quiescence on supershear segments has been previously observed and may reflect comparably homogeneous strength-stress conditions on geometrically simple and mature faults (Bouchon et al., 2010; Bouchon & Karabulut, 2008). In sharp contrast, the Maduo earthquake's gap of aftershocks encompasses a major step-over and several fault bends. While the second supershear transition also aligns with a gap in aftershocks, its signature is less clear in both optical data and our model, possibly due to the spatial proximity to geometric fault complexities.

The relative fault strength of our preferred scenario is highly heterogeneous ( $S$  ratio, Figure S8I in Supporting Information S1), with localized weak asperities and strong strength barriers. Moreover, the Jiangcuo fault that ruptured during the Maduo earthquake does not have a pronounced geomorphological expression and was only partly mapped before the occurrence of the event. Its cumulative long-term displacement has been measured at only two locations and is low ( $<5$  km, C. Li, Li, Shan, & Zhang, 2023). The fault's low geodetic slip rates ( $1.2 \pm 0.8$  mm/an, Y. Zhu et al., 2021) also suggest that this fault is likely immature.

While we discuss alternative models (Figures S12–S31 in Supporting Information S1), we cannot rule out that different geometry, friction, or off-fault parameterizations may reproduce the available observations of rupture characteristics equally well as our preferred model (e.g., Tinti et al., 2021). Denser and joint seismic, geodetic and optical time-dependent near-fault observations may help to shed light on dynamic trade-offs, for example, by enabling more direct constraints of  $D_{RS}$  (e.g., Mikumo et al., 2003), and better constraining the timing of rupture (e.g., Gabriel et al., 2023; S. Wang et al., 2022).

## 5. Conclusion

We demonstrate that an integrated analysis of an ensemble of multi-fault 3D dynamic rupture models, high-resolution optical correlation analysis, joint optical-InSAR-slip inversion, and validation by teleseismic observations can help to develop a fundamental understanding of the mechanical conditions that may have governed the complex dynamics of the 2021  $M_w$  7.4 Maduo earthquake. We extract high-resolution surface rupture traces from optical correlation and invert for a static slip model using InSAR and optical data, providing information on small-scale fault heterogeneous stress. Our preferred dynamic rupture model accounts for multi-segment fault geometry, varying dip angles along the fault, multi-scale stress heterogeneities, and variation in fault fracture energy. It can explain the event's complex kinematics, such as a multi-peak moment rate release, unilateral supershear rupture, and dynamic triggering of secondary branches. In the west, despite the modeled smoother fault morphology, dynamic rupture does not transition to supershear in our preferred model. This may be attributed to insufficient stress accumulation and local variations in fault friction properties, which might not favor supershear despite the smoother fault surface. In contrast, the unexpected transition to supershear in the east, sustained despite rupture jumping across the complex, more segmented fault system geometry, highlights the potential importance of fault heterogeneities and complex stress fields efficiently promoting supershear propagation under seemingly unfavorable conditions. Our understanding of the actual fault geometrical structure at depth is limited, being inferred from surface measurements. We explore the sensitivity of rupture dynamics to fault segmentation, tectonic prestress, off-fault plasticity, and frictional fault parameters. By comparing geodetic and dynamic rupture off-fault plastic damage measures, we identify observational signatures of supershear rupture. Our results imply that a high level of fault maturity, as well as homogeneous stress-strength conditions and geometric simplicity, may not necessarily be required preconditions for supershear rupture. This study opens new avenues to observe and better understand such - potentially not unusual - complex earthquake dynamics and their underlying driving factors.

## Conflict of Interest

The authors declare no conflicts of interest relevant to this study.

## Data Availability Statement

All data required to reproduce the 3D dynamic rupture scenarios, as well as the geodetic displacement fields (Sentinel-1, Sentinel-2, and SPOT6/7), the geodetic slip model, the SPOT 6/7 fault offsets, and the fault zone width estimates, are available at Zenodo (Hayek et al., 2024).

We use the SeisSol software package available on GitHub (<https://github.com/SeisSol/SeisSol>) to simulate all dynamic rupture models. We use SeisSol, version 202103\_Sumatra-686-gf8e01a54 (master branch on commit 9e8fa8a24dbc421a4b8395616bcab6a58e4cd4cd, v1.1.3, 2024). The procedure to download and run the code is described in the SeisSol documentation ([seissol.readthedocs.io/en/latest/](https://seissol.readthedocs.io/en/latest/)). Downloading and compiling instructions are at <https://seissol.readthedocs.io/en/latest/compiling-seissol.html>. Instructions for setting up and running simulations are at <https://seissol.readthedocs.io/en/latest/configuration.html>. Quickstart containerized installations and introductory materials are provided in the docker container and Jupyter Notebooks at <https://github.com/SeisSol/Training>. Example problems and model configuration files are provided at <https://github.com/SeisSol/Examples>, many of which reproduce the SCEC 3D Dynamic Rupture benchmark problems described at [https://strike.scec.org/cvws/benchmark\\_descriptions.html](https://strike.scec.org/cvws/benchmark_descriptions.html). The pseudo-dynamic simulation using a kinematic slip model on the fault to calculate fault stress heterogeneity is stated in the document (<https://seissol.readthedocs.io/en/latest/slip-rate-on-DR.html>).

We use the following projection for the dynamic simulation: EPSG:3415. The Global Positioning System (GPS) three-component coseismic offsets used to compare with our dynamic rupture model synthetics are from M. Wang et al. (2021). The Sentinel-2 optical images are freely available and were downloaded from the European Space Agency website (<https://dataspace.copernicus.eu/>). SAR Copernicus Sentinel-1 data captured by ESA are freely available and were downloaded from PEPS archive operated by CNES <https://peps.cnes.fr/rocket/#/home>.

InSAR data were pre-processed using the online service GDM-SAR supported by Formater (<https://www.poletteresolide.fr>), ISDeform (<https://www.isdeform.fr/>) and CNES (<https://cnes.fr/fr>).

## Acknowledgments

This work was supported by the European Union's Horizon 2020 research and innovation programme (TEAR ERC Starting; Grant 852992) and Horizon Europe (ChEESE-2P, Grant 101093038; DT-GEO, Grant 101058129; and Geo-INQUIRE, Grant 101058518), the National Science Foundation (Grant EAR-2225286, EAR-2121568, OAC-2139536, OAC-2311208), the National Aeronautics and Space Administration (Grant 80NSSC20K0495), and SCEC (project 24103). JH acknowledges financial support from the Agence Nationale de la Recherche (ANR) under Grant ANR-22-CE01-0028-01. We thank Solène Antoine, Chenglong Li, and Thomas Ulrich for valuable discussions. We acknowledge the Editor Germán Prieto, Ruth Harris, and one anonymous reviewer for their thoughtful and constructive comments.

## References

- Abdelmeguid, M., Zhao, C., Yalcinkaya, E., Gazetas, G., Elbanna, A., & Rosakis, A. (2023). Dynamics of episodic supershear in the 2023 M7.8 Kahramanmaraş/Pazarcik earthquake, revealed by near-field records and computational modeling. *Communications Earth & Environment*, 4(1), 456. <https://doi.org/10.1038/s43247-023-01131-7>
- Abercrombie, R. E. (2021). Resolution and uncertainties in estimates of earthquake stress drop and energy release. *Philosophical Transactions of the Royal Society A: Mathematical, Physical & Engineering Sciences*, 379(2196), 20200131. <https://doi.org/10.1098/rsta.2020.0131>
- Aki, K., & Richards, P. G. (2002). Quantitative seismology.
- Andrews, D. J. (1976). Rupture propagation with finite stress in antiplane strain. *Journal of Geophysical Research (1896-1977)*, 81(20), 3575–3582. <https://doi.org/10.1029/JB081i020p03575>
- Andrews, D. J. (1985). Dynamic plane-strain shear rupture with a slip-weakening friction law calculated by a boundary integral method. *Bulletin of the Seismological Society of America*, 75(1), 1–21. <https://doi.org/10.1785/BSSA0750010001>
- Andrews, D. J. (2005). Rupture dynamics with energy loss outside the slip zone. *Journal of Geophysical Research*, 110(B1), B01307. <https://doi.org/10.1029/2004JB003191>
- Antoine, S. L., Klinger, Y., Delorme, A., Wang, K., Bürgmann, R., & Gold, R. D. (2021). Diffuse deformation and surface faulting distribution from submetric image correlation along the 2019 Ridgecrest, California, ruptures. *Bulletin of the Seismological Society of America*, 111(5), 2275–2302. <https://doi.org/10.1785/0120210036>
- Biemiller, J., Gabriel, A.-A., & Ulrich, T. (2022). The dynamics of unlikely slip: 3D modeling of low-angle normal Fault Rupture at the Mai'iu fault, Papua New Guinea. *Geochemistry, Geophysics, Geosystems*, 23(5), e2021GC010298. <https://doi.org/10.1029/2021GC010298>
- Bouchon, M., & Karabulut, H. (2008). The aftershock signature of supershear earthquakes. *Science*, 320(5881), 1323–1325. <https://doi.org/10.1126/science.1155030>
- Bouchon, M., Karabulut, H., Bouin, M.-P., Schmitzbuhl, J., Vallée, M., Archuleta, R., et al. (2010). Faulting characteristics of supershear earthquakes. *Tectonophysics*, 493(3–4), 244–253. <https://doi.org/10.1016/j.tecto.2010.06.011>
- Burridge, R. (1973). Admissible speeds for plane-strain self-similar shear cracks with friction but lacking cohesion. *Geophysical Journal International*, 35(4), 439–455. <https://doi.org/10.1111/j.1365-246X.1973.tb00608.x>
- Cappa, F., Perrin, C., Manighetti, I., & Delor, E. (2014). Off-fault long-term damage: A condition to account for generic, triangular earthquake slip profiles. *Geochemistry, Geophysics, Geosystems*, 15(4), 1476–1493. <https://doi.org/10.1002/2013gc005182>
- Chen, K., Avouac, J.-P., Geng, J., Liang, C., Zhang, Z., Li, Z., & Zhang, S. (2022). The 2021 Mw 7.4 Madoi earthquake: An archetype bilateral slip-pulse rupture arrested at a splay fault. *Geophysical Research Letters*, 49(2), e2021GL095243. <https://doi.org/10.1029/2021GL095243>
- Cheng, C., Wang, D., Yao, Q., Fang, L., Xu, S., Huang, Z., et al. (2023). The 2021 Mw 7.3 Madoi, China earthquake: Transient supershear ruptures on a presumed immature strike-slip fault. *Journal of Geophysical Research: Solid Earth*, 128(2), e2022JB024641. <https://doi.org/10.1029/2022JB024641>
- Cocco, M., Aretusini, S., Cornelio, C., Nielsen, S. B., Spagnuolo, E., Tinti, E., & Di Toro, G. (2023). Fracture energy and breakdown work during earthquakes. *Annual Review of Earth and Planetary Sciences*, 51(1), 217–252. <https://doi.org/10.1146/annurev-earth-071822-100304>
- Delouis, B., van den Ende, M., & Ampuero, J.-P. (2023). Kinematic rupture model of the 6 February 2023  $M_w$  7.8 Türkiye earthquake from a large set of near-source strong-motion records combined with GNSS offsets reveals intermittent supershear rupture. *Bulletin of the Seismological Society of America*, 114(2), 726–740. <https://doi.org/10.1785/0120230077>

- Ding, K., Wang, Q., Li, Z., He, P., Zhang, P., Chen, J., et al. (2022). Rapid source determination of the 2021 Mw 7.4 Maduo earthquake by a dense high-rate GNSS network in the Tibetan plateau. *Seismological Research Letters*, 93(6), 3234–3245. <https://doi.org/10.1785/0220210307>
- Dunham, E. M. (2007). Conditions governing the occurrence of supershear ruptures under slip-weakening friction. *Journal of Geophysical Research*, 112(B7), B07302. <https://doi.org/10.1029/2006JB004717>
- Dunham, E. M., Belanger, D., Cong, L., & Kozdon, J. E. (2011a). Earthquake ruptures with strongly rate-weakening friction and off-fault plasticity, Part 1: Planar faults. *Bulletin of the Seismological Society of America*, 101(5), 2296–2307. <https://doi.org/10.1785/0120100075>
- Dunham, E. M., Belanger, D., Cong, L., & Kozdon, J. E. (2011b). Earthquake ruptures with strongly rate-weakening friction and off-fault plasticity, part 2: Nonplanar faults. *Bulletin of the Seismological Society of America*, 101(5), 2308–2322. <https://doi.org/10.1785/0120100076>
- Dziewonski, A. M., Chou, T.-A., & Woodhouse, J. H. (1981). Determination of earthquake source parameters from waveform data for studies of global and regional seismicity. *Journal of Geophysical Research*, 86(B4), 2825–2852. <https://doi.org/10.1029/JB086iB04p02825>
- Ekström, G., Nettles, M., & Dziewoński, A. (2012). The global CMT project 2004–2010: Centroid-moment tensors for 13,017 earthquakes. *Physics of the Earth and Planetary Interiors*, 200–201, 1–9. <https://doi.org/10.1016/j.pepi.2012.04.002>
- Fan, X., Zhang, G., Zhao, D., Xie, C., Huang, C., & Shan, X. (2022). Fault geometry and kinematics of the 2021 Mw 7.3 Maduo earthquake from aftershocks and InSAR observations. *Frontiers in Earth Science*, 10. <https://doi.org/10.3389/feart.2022.993984>
- Fang, J., Ou, Q., Wright, T. J., Okuwaki, R., Amey, R. M., Craig, T. J., et al. (2022). Earthquake cycle deformation associated with the 2021 Mw 7.4 Maduo (Eastern Tibet) earthquake: An intrablock rupture event on a slow-slipping fault from Sentinel-1 InSAR and teleseismic data. *Journal of Geophysical Research: Solid Earth*, 127(11), e2022JB024268. <https://doi.org/10.1029/2022jb024268>
- Fialko, Y., Sandwell, D., Simons, M., & Rosen, P. (2005). Three-dimensional deformation caused by the Bam, Iran, earthquake and the origin of shallow slip deficit. *Nature*, 435(7040), 295–299. <https://doi.org/10.1038/nature03425>
- Gabriel, A.-A., Ampuero, J.-P., Dalguer, L. A., & Mai, P. M. (2012). The transition of dynamic rupture styles in elastic media under velocity-weakening friction. *Journal of Geophysical Research*, 117(B9), B09311. <https://doi.org/10.1029/2012JB009468>
- Gabriel, A.-A., Ulrich, T., Marchandon, M., Biemiller, J., & Rekoske, J. (2023). 3D dynamic rupture modeling of the 6 February 2023, Kahramanmaraş, Turkey Mw 7.8 and 7.7 earthquake doublet using early observations. *The Seismic Record*, 3(4), 342–356. <https://doi.org/10.1785/0320230028>
- Gao, Z., Li, Y., Shan, X., & Zhu, C. (2021). Earthquake magnitude estimation from high-rate GNSS data: A case study of the 2021 Mw 7.3 Maduo earthquake. *Remote Sensing*, 13(21), 4478. <https://doi.org/10.3390/rs13214478>
- Guo, R., Yang, H., Li, Y., Zheng, Y., & Zhang, L. (2021). Complex slip distribution of the 2021 Mw 7.4 Maduo, China, earthquake: An event occurring on the slowly slipping fault. *Seismological Research Letters*, 93(2A), 653–665. <https://doi.org/10.1785/0220210226>
- Hamling, I. J., Hreinsdóttir, S., Clark, K., Elliott, J., Liang, C., Fielding, E., et al. (2017). Complex multifault rupture during the 2016 Mw 7.8 Kaikōura earthquake, New Zealand. *Science*, 356(6334), eaam7194. <https://doi.org/10.1126/science.aam7194>
- Harris, R. A., Barall, M., Aagaard, B., Ma, S., Roten, D., Olsen, K., et al. (2018). A suite of exercises for verifying dynamic earthquake rupture codes. *Seismological Research Letters*, 89(3), 1146–1162. <https://doi.org/10.1785/0220170222>
- Hauksson, E., Jones, L. M., Hutton, K., & Eberhart-Phillips, D. (1993). The 1992 Landers earthquake sequence: Seismological observations. *Journal of Geophysical Research*, 98(B11), 19835–19858. <https://doi.org/10.1029/93JB02384>
- Hayek, J. N., Marchandon, M., Li, D., Pousse-Beltran, L., Hollingsworth, J., Li, T., & Gabriel, A.-A. (2024). SeisSol input files and geodetic results for “non-typical supershear rupture: Fault heterogeneity and segmentation govern unilateral supershear and cascading multi-fault rupture in the 2021 Mw 7.4 Maduo earthquake [Dataset]. *Zenodo*. <https://doi.org/10.5281/zenodo.13589206>
- He, K., Wen, Y., Xu, C., & Zhao, Y. (2021a). Fault geometry and slip distribution of the 2021 Mw 7.4 Maduo, China, earthquake inferred from InSAR measurements and relocated aftershocks. *Seismological Research Letters*, 93(1), 8–20. <https://doi.org/10.1785/0220210204>
- He, L., Feng, G., Wu, X., Lu, H., Xu, W., Wang, Y., et al. (2021b). Coseismic and early postseismic slip models of the 2021 Mw 7.4 Maduo earthquake (Western China) estimated by space-based geodetic data. *Geophysical Research Letters*, 48(24), e2021GL095860. <https://doi.org/10.1029/2021GL095860>
- Heinecke, A., Breuer, A., Rettenberger, S., Bader, M., Gabriel, A.-A., Pelties, C., et al. (2014). Petascale high order dynamic rupture earthquake simulations on heterogeneous supercomputers. In *SC '14: Proceedings of the international conference for high performance computing, networking, storage and analysis* (pp. 3–14). <https://doi.org/10.1109/SC.2014.6>
- Hu, F., Oglesby, D. D., & Chen, X. (2021). The effect of depth-dependent stress in controlling free-surface-induced supershear rupture on strike-slip faults. *Journal of Geophysical Research: Solid Earth*, 126(5), e2020JB021459. <https://doi.org/10.1029/2020JB021459>
- Hu, F., Xu, J., Zhang, Z., & Chen, X. (2016). Supershear transition mechanism induced by step over geometry. *Journal of Geophysical Research: Solid Earth*, 121(12), 8738–8749. <https://doi.org/10.1002/2016JB013333>
- Huang, L., Zhang, B., & Shi, Y. (2021). Stress transfer at the northeastern end of the Bayan Har block and its implications for seismic hazards: Insights from numerical simulations. *Earth and Space Science*, 8(12), e2021EA001947. <https://doi.org/10.1029/2021EA001947>
- Huang, Y., Ampuero, J.-P., & Helmlinger, D. V. (2014). Earthquake ruptures modulated by waves in damaged fault zones. *Journal of Geophysical Research: Solid Earth*, 119(4), 3133–3154. <https://doi.org/10.1002/2013jb010724>
- Jara, J., Bruhat, L., Thomas, M. Y., Antoine, S. L., Okubo, K., Rougier, E., et al. (2021). Signature of transition to supershear rupture speed in the coseismic off-fault damage zone. *Proceedings of the Royal Society A: Mathematical, Physical & Engineering Sciences*, 477(2255), 20210364. <https://doi.org/10.1098/rspa.2021.0364>
- Jia, Z., Jin, Z., Marchandon, M., Ulrich, T., Gabriel, A.-A., Fan, W., et al. (2023). The complex dynamics of the 2023 Kahramanmaraş, Turkey, Mw 7.8–7.7 earthquake doublet. *Science*, 381(0), eadi0685–990. <https://doi.org/10.1126/science.adi0685>
- Jin, Z., & Fialko, Y. (2021). Coseismic and early postseismic deformation due to the 2021 M7.4 Maduo (China) earthquake. *Geophysical Research Letters*, 48(21), e2021GL095213. <https://doi.org/10.1029/2021GL095213>
- Jin, Z., Fialko, Y., Yang, H., & Li, Y. (2023). Transient deformation excited by the 2021 M7.4 Maduo (China) earthquake: Evidence of a deep shear zone. *Journal of Geophysical Research: Solid Earth*, 128(8), e2023JB026643. <https://doi.org/10.1029/2023JB026643>
- Kaneko, Y., & Fialko, Y. (2011). Shallow slip deficit due to large strike-slip earthquakes in dynamic rupture simulations with elasto-plastic off-fault response. *Geophysical Journal International*, 186(3), 1389–1403. <https://doi.org/10.1111/j.1365-246X.2011.05117.x>
- Kaneko, Y., & Lapusta, N. (2010). Supershear transition due to a free surface in 3-D simulations of spontaneous dynamic rupture on vertical strike-slip faults. *Tectonophysics*, 493(3), 272–284. <https://doi.org/10.1016/j.tecto.2010.06.015>
- Käser, M., & Dumbser, M. (2006). An arbitrary high-order discontinuous Galerkin method for elastic waves on unstructured meshes — I. The two-dimensional isotropic case with external source terms. *Geophysical Journal International*, 166(2), 855–877. <https://doi.org/10.1111/j.1365-246X.2006.03051.x>
- Li, C., Li, T., Hollingsworth, J., Zhang, Y., Qian, L., & Shan, X. (2023a). Strain threshold for the formation of coseismic surface rupture. *Geophysical Research Letters*, 50(16), e2023GL103666. <https://doi.org/10.1029/2023gl103666>

- Li, C., Li, T., Shan, X., & Zhang, G. (2023b). Extremely large off-fault deformation during the 2021 Mw 7.4 Maduo, Tibetan Plateau, Earthquake. *Seismological Society of America*, 94(1), 39–51. <https://doi.org/10.1785/0220220139>
- Li, Q., Wan, Y., Li, C., Tang, H., Tan, K., & Wang, D. (2022). Source process featuring asymmetric rupture velocities of the 2021 Mw 7.4 Maduo, China, earthquake from teleseismic and geodetic data. *Seismological Research Letters*, 93(3), 1429–1439. <https://doi.org/10.1785/0220210300>
- Liu-Zeng, J., Liu, Z., Liu, X., Milliner, C., Rodriguez Padilla, A. M., Xu, S., et al. (2024). Fault orientation trumps fault maturity in controlling coseismic rupture characteristics of the 2021 Maduo earthquake. *AGU Advances*, 5(2), e2023AV001134. <https://doi.org/10.1029/2023AV001134>
- Lyu, M., Chen, K., Xue, C., Zang, N., Zhang, W., & Wei, G. (2022). Overall subshear but locally supershear rupture of the 2021 Mw 7.4 Maduo earthquake from high-rate GNSS waveforms and three-dimensional InSAR deformation. *Tectonophysics*, 839, 229542. <https://doi.org/10.1016/j.tecto.2022.229542>
- Ma, H., Feng, J., Wang, Q., Zhao, J., Zou, Z., Yuan, Z., & Li, M. (2022). Stress and strain characteristics before the Mw 7.3 Maduo earthquake and its implications for future earthquakes on the Maqin–Maqu fault. *Bulletin of the Seismological Society of America*, 112(5), 2454–2467. <https://doi.org/10.1785/0120210219>
- Ma, S. (2008). A physical model for widespread near-surface and fault zone damage induced by earthquakes. *Geochemistry, Geophysics, Geosystems*, 9(11), Q11009. <https://doi.org/10.1029/2008GC002231>
- Manighetti, I., Caulet, C., Barros, L. D., Perrin, C., Cappa, F., & Gaudemer, Y. (2015). Generic along-strike segmentation of Afar normal faults, East Africa: Implications on fault growth and stress heterogeneity on seismogenic fault planes. *Geochemistry, Geophysics, Geosystems*, 16(2), 443–467. <https://doi.org/10.1002/2014GC005691>
- Mikumo, T., Olsen, K. B., Fukuyama, E., & Yagi, Y. (2003). Stress-Breakdown time and slip-weakening distance inferred from slip-velocity functions on earthquake faults. *Bulletin of the Seismological Society of America*, 93(1), 264–282. <https://doi.org/10.1785/0120020082>
- Milliner, C. W. D., Dolan, J. F., Hollingsworth, J., Leprince, S., Ayoub, F., & Sammis, C. G. (2015). Quantifying near-field and off-fault deformation patterns of the 1992 Mw 7.3 Landers earthquake. *Geochemistry, Geophysics, Geosystems*, 16(5), 1577–1598. <https://doi.org/10.1002/2014GC005693>
- Nevitt, J. M., Brooks, B. A., Catchings, R. D., Goldman, M. R., Erickson, T. L., & Glennie, C. L. (2020). Mechanics of near-field deformation during co- and post-seismic shallow fault slip. *Scientific Reports*, 10(1), 5031. <https://doi.org/10.1038/s41598-020-61400-9>
- Pan, J., Li, H., Chevalier, M.-L., Tapponnier, P., Bai, M., Li, C., et al. (2022). Co-seismic rupture of the 2021, Mw7.4 Maduo earthquake (northern Tibet): Short-cutting of the Kunlun fault big bend. *Earth and Planetary Science Letters*, 594, 117703. <https://doi.org/10.1016/j.epsl.2022.117703>
- Pelties, C., Gabriel, A.-A., & Ampuero, J.-P. (2014). Verification of an ADER-DG method for complex dynamic rupture problems. *Geoscientific Model Development*, 7(3), 847–866. <https://doi.org/10.5194/gmd-7-847-2014>
- Perrin, C., Manighetti, I., & Gaudemer, Y. (2016). Off-fault tip splay networks: A genetic and generic property of faults indicative of their long-term propagation. *Comptes Rendus Geoscience*, 348(1), 52–60. <https://doi.org/10.1016/j.crte.2015.05.002>
- Ramos, M. D., Thakur, P., Huang, Y., Harris, R. A., & Ryan, K. J. (2022). Working with dynamic earthquake rupture models: A practical guide. *Seismological Research Letters*, 93(4), 2096–2110. <https://doi.org/10.1785/0220220022>
- Ren, J., Zhang, Z., Gai, H., & Kang, W. (2021). Typical Riedel shear structures of the coseismic surface rupture zone produced by the 2021 Mw 7.3 Maduo earthquake, Qinghai, China, and the implications for seismic hazards in the block interior. *Natural Hazards Research*, 1(4), 145–152. <https://doi.org/10.1016/j.nhres.2021.10.001>
- Rodriguez Padilla, A. M., & Oskin, M. E. (2023). Displacement hazard from distributed ruptures in strike-slip earthquakes. *Bulletin of the Seismological Society of America*, 113(6), 2730–2745. <https://doi.org/10.1785/0120230044>
- Ross, Z. E., Idini, B., Jia, Z., Stephenson, O. L., Zhong, M., Wang, X., et al. (2019). Hierarchical interlocked orthogonal faulting in the 2019 Ridgecrest earthquake sequence. *Science*, 366(6463), 346–351. <https://doi.org/10.1126/science.aaz0109>
- Roten, D., Olsen, K. B., & Day, S. M. (2017). Off-fault deformations and shallow slip deficit from dynamic rupture simulations with fault zone plasticity. *Geophysical Research Letters*, 44(15), 7733–7742. <https://doi.org/10.1002/2017gl074323>
- Roten, D., Olsen, K. B., Day, S. M., Cui, Y., & Fäh, D. (2014). Expected seismic shaking in Los Angeles reduced by San Andreas fault zone plasticity. *Geophysical Research Letters*, 41(8), 2769–2777. <https://doi.org/10.1002/2014GL059411>
- Schwartz, D. P., & Coppersmith, K. J. (1984). Fault behavior and characteristic earthquakes: Examples from the Wasatch and San Andreas fault zones. *Journal of Geophysical Research*, 89(B7), 5681–5698. <https://doi.org/10.1029/JB089iB07p05681>
- Scott, C. P., Arrowsmith, J. R., Nissen, E., Lajoie, L., Maruyama, T., & Chiba, T. (2018). The M7 2016 Kumamoto, Japan, earthquake: 3-D deformation along the fault and within the damage zone constrained from differential lidar topography. *Journal of Geophysical Research: Solid Earth*, 123(7), 6138–6155. <https://doi.org/10.1029/2018jb015581>
- Simons, M., Fialko, Y., & Rivera, L. (2002). Coseismic deformation from the 1999 Mw 7.1 Hector Mine, California, earthquake as inferred from InSAR and GPS observations. *Bulletin of the Seismological Society of America*, 92(4), 1390–1402. <https://doi.org/10.1785/0120000933>
- Styron, R., Taylor, M., & Okoronkwo, K. (2010). Database of active structures from the Indo-Asian Collision. *Eos, Transactions American Geophysical Union*, 91(20), 181–182. <https://doi.org/10.1029/2010EO200001>
- Tang, R., Yuan, J., & Gan, L. (2021). Free-surface-induced supershear transition in 3-D simulations of spontaneous dynamic rupture on oblique faults. *Geophysical Research Letters*, 48(3), e2020GL091621. <https://doi.org/10.1029/2020GL091621>
- Taufiqurrahman, T., Gabriel, A.-A., Li, D., Ulrich, T., Li, B., Carena, S., et al. (2023). Dynamics, interactions and delays of the 2019 Ridgecrest rupture sequence. *Nature*, 618(7964), 308–315. <https://doi.org/10.1038/s41586-023-05985-x>
- Templeton, E. L., & Rice, J. R. (2008). Off-fault plasticity and earthquake rupture dynamics: 1. Dry materials or neglect of fluid pressure changes. *Journal of Geophysical Research*, 113(B09306). <https://doi.org/10.1029/2007JB005529>
- Tinti, E., Casarotti, E., Ulrich, T., Taufiqurrahman, T., Li, D., & Gabriel, A.-A. (2021). Constraining families of dynamic models using geological, geodetic and strong ground motion data: The Mw 6.5, October 30th, 2016, Norcia earthquake, Italy. *Earth and Planetary Science Letters*, 576, 117237. <https://doi.org/10.1016/j.epsl.2021.117237>
- Ulrich, T., Gabriel, A.-A., Ampuero, J.-P., & Xu, W. (2019). Dynamic viability of the 2016 Mw 7.8 Kaikōura earthquake cascade on weak crustal faults. *Nature Communications*, 10(1), 1213. <https://doi.org/10.1038/s41467-019-09125-w>
- UNICEF China. (2021). UNICEF sends supplies to children affected by an earthquake in Qinghai province. Retrieved from <https://www.unicef.cn/en/press-releases/unicef-sends-supplies-children-affected-earthquake-qinghai-province>
- Uphoff, C., Rettenberger, S., Bader, M., Madden, E. H., Ulrich, T., Wollherr, S., & Gabriel, A.-A. (2017). Extreme scale multi-physics simulations of the tsunamigenic 2004 Sumatra megathrust earthquake. In *Proceedings of the international conference for high performance computing, networking, storage and analysis*. Association for Computing Machinery. <https://doi.org/10.1145/3126908.3126948>
- USGS. (2021). Overview: M7.3 - Southern Qinghai, China. Retrieved from <https://earthquake.usgs.gov/earthquakes/eventpage/us7000e54r/executive>

- Wang, M., Wang, F., Jiang, X., Tian, J., Li, Y., Sun, J., & Shen, Z.-K. (2021a). GPS determined coseismic slip of the 2021 Mw 7.4 Maduo, China, earthquake and its tectonic implication. *Geophysical Journal International*, 228(3), 2048–2055. <https://doi.org/10.1093/gji/ggab460>
- Wang, S., Song, C., Li, S., & Li, X. (2022). Resolving co-and early post-seismic slip variations of the 2021 Mw 7.4 Madoi earthquake in east Bayan Har block with a block-wide distributed deformation mode from satellite synthetic aperture radar data. *Earth Planet. Phys.*, 6(1), 108–122. <https://doi.org/10.26464/epp2022007>
- Wang, W., Fang, L., Wu, J., Tu, H., Chen, L., Lai, G., & Zhang, L. (2021b). Aftershock sequence relocation of the 2021 Ms 7.4 Maduo earthquake, Qinghai, China. *Science China Earth Sciences*, 64(8), 1371–1380. <https://doi.org/10.1007/s11430-021-9803-3>
- Wei, G., Chen, K., Lyu, M., Gong, W., Dal Zilio, L., Ye, L., & Tu, H. (2023). Complex strike-slip faulting during the 2021 Mw7.4 Maduo earthquake. *Communications Earth & Environment*, 4(1), 319. <https://doi.org/10.1038/s43247-023-00980-6>
- Wei, S., Zeng, H., Shi, Q., Liu, J., Luo, H., Hu, W., et al. (2022). Simultaneous rupture propagation through fault bifurcation of the 2021 Mw 7.4 Maduo earthquake. *Geophysical Research Letters*, 49(21), e2022GL100283. <https://doi.org/10.1029/2022GL100283>
- Wen, Y., Cai, J., He, K., & Xu, C. (2024). Dynamic rupture of the 2021 MW 7.4 Maduo earthquake: An intra-block event controlled by fault geometry. *Journal of Geophysical Research*, 129(1), e2023JB027247. <https://doi.org/10.1029/2023JB027247>
- Wollherr, S., Gabriel, A.-A., & Mai, P. M. (2019). Landers 1992 “reloaded”: Integrative dynamic earthquake rupture modeling. *Journal of Geophysical Research: Solid Earth*, 124(7), 6666–6702. <https://doi.org/10.1029/2018JB016355>
- Wollherr, S., Gabriel, A.-A., & Uphoff, C. (2018). Off-fault plasticity in three-dimensional dynamic rupture simulations using a modal discontinuous Galerkin method on unstructured meshes: Implementation, verification and application. *Geophysical Journal International*, 214(3), 1556–1584. <https://doi.org/10.1093/GJI/GGY213>
- Xin, H., Zhang, H., Kang, M., He, R., Gao, L., & Gao, J. (2018). High-resolution lithospheric velocity structure of continental China by double-difference seismic travel-time tomography. *Seismological Research Letters*, 90(1), 229–241. <https://doi.org/10.1785/0220180209>
- Xu, B., & Zhang, Y. (2023). Joint inversion of centroid moment tensor for large earthquakes by combining teleseismic P-wave and W-phase records. *Geophysical Journal International*, 234(2), 1143–1156. <https://doi.org/10.1093/gji/ggad128>
- Xu, J., Zhang, H., & Chen, X. (2015). Rupture phase diagrams for a planar fault in 3-D full-space and half-space. *Geophysical Journal International*, 202(3), 2194–2206. <https://doi.org/10.1093/gji/ggv284>
- Yuan, J., & Li, Y. (2023). Complex fault geometry controls dynamic rupture of the 2021 Mw7.4 Maduo earthquake, NE Tibetan Plateau. *Tectonophysics*, 868, 230105. <https://doi.org/10.1016/j.tecto.2023.230105>
- Yuan, Z., Li, T., Su, P., Sun, H., Ha, G., Guo, P., et al. (2022). Large surface-rupture gaps and low Surface Fault slip of the 2021 Mw 7.4 Maduo earthquake along a low-activity strike-slip fault, Tibetan plateau. *Geophysical Research Letters*, 49(6), e2021GL096874. <https://doi.org/10.1029/2021GL096874>
- Yue, H., Shen, Z.-K., Zhao, Z., Wang, T., Cao, B., Li, Z., et al. (2022). Rupture process of the 2021 M7.4 Maduo earthquake and implication for deformation mode of the Songpan-Ganzi terrane in Tibetan Plateau. *Proceedings of the National Academy of Sciences*, 119(23), e2116445119. <https://doi.org/10.1073/pnas.2116445119>
- Zhang, P., Deng, Q., Zhang, G., Ma, J., Gan, W., Min, W., et al. (2003). Active tectonic blocks and strong earthquakes in the continent of China. *Science in China - Series D: Earth Sciences*, 46(2), 13–24. <https://doi.org/10.1360/03dz0002>
- Zhang, X., Feng, W., Du, H., Samsonov, S., & Yi, L. (2022). Supershear rupture during the 2021 Mw 7.4 Maduo, China, earthquake. *Geophysical Research Letters*, 49(6), e2022GL097984. <https://doi.org/10.1029/2022GL097984>
- Zhao, D., Qu, C., Chen, H., Shan, X., Song, X., & Gong, W. (2021). Tectonic and geometric control on fault kinematics of the 2021 Mw7.3 Maduo (China) earthquake inferred from interseismic, coseismic, and postseismic InSAR observations. *Geophysical Research Letters*, 48(18), e2021GL095417. <https://doi.org/10.1029/2021GL095417>
- Zhu, M., Chen, F., Fu, B., Chen, W., Qiao, Y., Shi, P., et al. (2023). Earthquake-induced risk assessment of cultural heritage based on InSAR and seismic intensity: A case study of Zhalang temple affected by the 2021 Mw 7.4 Maduo (China) earthquake. *International Journal of Disaster Risk Reduction*, 84, 103482. <https://doi.org/10.1016/j.ijdrr.2022.103482>
- Zhu, Y., Diao, F., Fu, Y., Liu, C., & Xiong, X. (2021). Slip rate of the seismogenic fault of the 2021 Maduo earthquake in western China inferred from GPS observations. *Science China Earth Sciences*, 64(8), 1363–1370. <https://doi.org/10.1007/s11430-021-9808-0>

## References From the Supporting Information

- Amante, C., & Eakins, B. W. (2009). ETOPO1 global relief model converted to PanMap layer format [Dataset]. *PANGAEA*. <https://doi.org/10.1594/PANGAEA.769615>
- Aochi, H., & Madariaga, R. (2003). The 1999 Izmit, Turkey, earthquake: Nonplanar fault structure, dynamic rupture process, and strong ground motion. *Bulletin of the Seismological Society of America*, 93(3), 1249–1266. <https://doi.org/10.1785/0120020167>
- Breuer, A., Heinecke, A., Rettenberger, S., Bader, M., Gabriel, A.-A., & Pelties, C. (2014). Sustained petascale performance of seismic simulations with SeisSol on SuperMUC. In J. M. Kunkel, T. Ludwig, & H. W. Meuer (Eds.), *Supercomputing* (pp. 1–18). Springer International Publishing.
- Coleman, T. F., & Li, Y. (1992). A globally and quadratically convergent affine scaling method for linear 1 problems. *Mathematical Programming*, 56(1–3), 189–222. <https://doi.org/10.1007/bf01580899>
- Day, S. M., Dalguer, L. A., Lapusta, N., & Liu, Y. (2005). Comparison of finite difference and boundary integral solutions to three-dimensional spontaneous rupture. *Journal of Geophysical Research*, 110(B12). <https://doi.org/10.1029/2005JB003813>
- Doin, M.-P., Lodge, F., Guillaso, S., Jolivet, R., Lasserre, C., Ducret, G., et al. (2011). Presentation of the small baseline NSBAS processing chain on a case example: The Etna deformation monitoring from 2003 to 2010 using EN data. In *Fringe symposium*.
- Doin, M.-P., Twardzik, C., Ducret, G., Lasserre, C., Guillaso, S., & Jianbao, S. (2015). InSAR measurement of the deformation around Siling Co Lake: Inferences on the lower crust viscosity in central Tibet. *Journal of Geophysical Research: Solid Earth*, 120(7), 5290–5310. <https://doi.org/10.1002/2014jb011768>
- Dumbser, M., & Käser, M. (2006). An arbitrary high-order discontinuous Galerkin method for elastic waves on unstructured meshes — II. The three-dimensional isotropic case. *Geophysical Journal International*, 167(1), 319–336. <https://doi.org/10.1111/j.1365-246X.2006.03120.x>
- Farr, T. G., Rosen, P. A., Caro, E., Crippen, R., Duren, R., Hensley, S., et al. (2007). The shuttle radar topography mission. *Reviews of Geophysics*, 45(2), RG2004. <https://doi.org/10.1029/2005rg000183>
- Gabriel, A.-A., Ampuero, J.-P., Dalguer, L. A., & Mai, P. M. (2013). Source properties of dynamic rupture pulses with off-fault plasticity. *Journal of Geophysical Research: Solid Earth*, 118(8), 4117–4126. <https://doi.org/10.1002/jgrb.50213>
- Grandin, R., Doin, M.-P., Bollinger, L., Pinel-Puysségur, B., Ducret, G., Jolivet, R., & Sapkota, S. N. (2012). Long-term growth of the Himalaya inferred from interseismic InSAR measurement. *Geology*, 40(12), 1059–1062. <https://doi.org/10.1130/g33154.1>

- Grandin, R., Socquet, A., Binet, R., Klinger, Y., Jacques, E., De Chabaliere, J.-B., et al. (2009). September 2005 Manda Hararo-Dabbahu rifting event, Afar (Ethiopia): Constraints provided by geodetic data. *Journal of Geophysical Research*, *114*(B8), B08404. <https://doi.org/10.1029/2008JB005843>
- Harris, R. A., Barall, M., Archuleta, R., Dunham, E., Aagaard, B., Ampuero, J. P., et al. (2009). The SCEC/USGS dynamic earthquake rupture code verification exercise. *Seismological Research Letters*, *80*(1), 119–126. <https://doi.org/10.1785/gssrl.80.1.119>
- Harris, R. A., & Day, S. M. (1993). Dynamics of fault interaction: Parallel strike-slip faults. *Journal of Geophysical Research*, *98*(B3), 4461–4472. <https://doi.org/10.1029/92JB02272>
- Harris, R. A., & Segall, P. (1987). Detection of a locked zone at depth on the Parkfield, California, segment of the San Andreas fault. *Journal of Geophysical Research*, *92*(B8), 7945–7962. <https://doi.org/10.1029/jb092ib08p07945>
- Jónsson, S., Zebker, H., Segall, P., & Amelung, F. (2002). Fault slip distribution of the 1999 Mw 7.1 Hector Mine, California, earthquake, estimated from satellite radar and GPS measurements. *Bulletin of the Seismological Society of America*, *92*(4), 1377–1389. <https://doi.org/10.1785/0120000922>
- Krenz, L., Uphoff, C., Ulrich, T., Gabriel, A.-A., Abrahams, L. S., Dunham, E. M., & Bader, M. (2021). 3D acoustic-elastic coupling with gravity: The dynamics of the 2018 Palu, Sulawesi earthquake and tsunami. In *Proceedings of the international conference for high performance computing, networking, storage and analysis*. Association for Computing Machinery. <https://doi.org/10.1145/3458817.3476173>
- Leprince, S., Barbot, S., Ayoub, F., & Avouac, J.-P. (2007). Automatic and precise orthorectification, coregistration, and subpixel correlation of satellite images, application to ground deformation measurements. *IEEE Transactions on Geoscience and Remote Sensing*, *45*(6), 1529–1558. <https://doi.org/10.1109/tgrs.2006.888937>
- Lohman, R. B., & Simons, M. (2005). Some thoughts on the use of InSAR data to constrain models of surface deformation: Noise structure and data downsampling. *Geochemistry, Geophysics, Geosystems*, *6*(1), Q01007. <https://doi.org/10.1029/2004gc000841>
- Madden, E. H., Ulrich, T., & Gabriel, A.-A. (2022). The state of pore fluid pressure and 3-D megathrust earthquake dynamics. *Journal of Geophysical Research: Solid Earth*, *127*(4), e2021JB023382. <https://doi.org/10.1029/2021JB023382>
- Maneewongvatana, S., & Mount, D. (1999). It's okay to be skinny, if your friends are fat. In *Center for geometric computing 4th annual workshop on computational geometry*.
- Marchandon, M., Vergnolle, M., Sudhaus, H., & Cavalié, O. (2018). Fault geometry and slip distribution at depth of the 1997 Mw 7.2 Zirkuh earthquake: Contribution of near-field displacement data. *Journal of Geophysical Research: Solid Earth*, *123*(2), 1904–1924. <https://doi.org/10.1002/2017JB014703>
- Meade, B. J. (2007). Algorithms for the calculation of exact displacements, strains, and stresses for triangular dislocation elements in a uniform elastic half space. *Computers & Geosciences*, *33*(8), 1064–1075. <https://doi.org/10.1016/j.cageo.2006.12.003>
- Pelties, C., de la Puente, J., Ampuero, J.-P., Brietzke, G. B., & Käser, M. (2012). Three-dimensional dynamic rupture simulation with a high-order discontinuous Galerkin method on unstructured tetrahedral meshes. *Journal of Geophysical Research*, *117*(B2), B02309. <https://doi.org/10.1029/2011JB008857>
- Scholz, C. H. (1988). The brittle-plastic transition and the depth of seismic faulting. *Geologische Rundschau*, *77*(1), 319–328. <https://doi.org/10.1007/BF01848693>
- Simmetrix Inc. (2017). *Simmodeler: Simulation modeling suite 11.0 documentation*. (Tech. Rep.). Simmetrix Inc.
- Thollard, F., Clesse, D., Doin, M.-P., Donadieu, J., Durand, P., Grandin, R., et al. (2021). Flatsim: The ForM@Ter Large-scale multi-temporal sentinel-1 Interferometry service. *Remote Sensing*, *13*(18), 3734. <https://doi.org/10.3390/rs13183734>
- Virtanen, P., Gommers, R., Oliphant, T. E., Haberland, M., Reddy, T., Cournapeau, D., et al., SciPy 1.0 Contributors (2020). SciPy 1.0: Fundamental algorithms for scientific computing in Python. *Nature Methods*, *17*(3), 261–272. <https://doi.org/10.1038/s41592-019-0686-2>
- Weng, H., & Yang, H. (2018). Constraining frictional properties on fault by dynamic rupture simulations and near-field observations. *Journal of Geophysical Research: Solid Earth*, *123*(8), 6658–6670. <https://doi.org/10.1029/2017JB015414>
- Wright, T. J., Lu, Z., & Wicks, C. (2003). Source model for the Mw 6.7, 23 October 2002, Nenana mountain earthquake (Alaska) from InSAR. *Geophysical Research Letters*, *30*(18). <https://doi.org/10.1029/2003gl018014>
- Zinke, R., Hollingsworth, J., Dolan, J. F., & Van Dissen, R. (2019). Three-dimensional surface deformation in the 2016 MW 7.8 Kaikōura, New Zealand, earthquake from optical image correlation: Implications for strain localization and long-term evolution of the Pacific-Australian plate boundary. *Geochemistry, Geophysics, Geosystems*, *20*(3), 1609–1628. <https://doi.org/10.1029/2018GC007951>